Supplementary Information for

"Effects of Catalyst Droplets on Wire Growth and Resulting Branched Structures during VLS Growth"

Miao Song,[a] Youtian Zhang[b], Jaehun Chun[a], Shenyang Hu[c], Ming Tang[b], Dongsheng Li[a]*

[a] *Physical and Computational Sciences Directorate, Pacific Northwest National Laboratory, Richland, WA 99352, USA. E-mail: Dongsheng.Li2@pnnl.gov*

[b] *Department of Materials Science and NanoEngineering, Rice University, Houston, TX 77024, USA.*

[c] *Energy and Environment Directorate, Pacific Northwest National Laboratory, Richland, WA 99352, USA*

* E-mail: Dongsheng.Li2@pnnl.gov

This file includes:

    Supplementary Text

    Movie S1. Nucleation and growth processes of catalyst droplets on sidewall of PbSe wires.

    Figs. S1 to S9

1. Experimental

The catalyst bismuth powder (Bi, purity ≥99.99%, Sigma-Aldrich) and the precursor material lead selenide (PbSe, purity 99.99%, Sigma-Aldrich) were grounded and dispersed in ethanol at a molar ratio of 1/5. The liquid was then drop-cast onto SiNx TEM heating chips. During our in-situ low magnification (LM) TEM experiment, a 652 furnace heating holder (Gatan, USA) was used. We found that PbSe wire grew only at a temperature higher than ~580 °Cin our experimental conditions. The accuracy of the temperature calibration is within ± ~25Fig.C. To grow PbSe hierarchical structures, a multi-step growth process was employed, and detailed steps are as follows: (1) Precursor powders were sandwiched by a SiN_x TEM chip and a carbon grid (or another SiNx chip). The sandwiched cell was heated up to 600°C or 605°C in N_2 environment at a pressure of ~5×10^2 Pa for the first PbSe wire growth; (2) After the first growth, TEM grids were cooled to room temperature, and additional Bi powders were added to the cell. The carbon grid (or one of the SiNx chip) was replaced with a new one for imaging purposes. One used SiNx chip was kept with numerous of PbSe wires and PbSe precursors. The reassembled cell was heated to 600 °C or 605°C again for the secondary branch growth; (3) Repeating step (2) for the further growth of PbSe hierarchical structures. Notably, although the ratio of the amount of the growth precursors of Bi to PbSe employed in our experiment was roughly 1 to 5, the exact vapor concentration of precursors between two TEM grids was unclear.

The temperature ramping rate cannot be controlled digitally. The temperature is controlled by setting the desired temperature and the heating unit increases the temperature as fast as possible. The ramping rate depends on difference between the initial and end temperatures. Therefore, to kinetically control the wire growth process, we tuned heating process via three paths. In order to keep the ramping rate the same before the reaction occurs, the temperature was increased to 580°Cfirst from room temperature for all three experiments. For experiment 1, to slow the heating rate (Fig. 1h-k and Fig. 2a-h), the temperature was held at 580 °C for 1 min, then increased to 590 °C and 600 °C step-by-step for PbSe wire

growth. For experiment 2 (Fig. S2), to increase the ramping rate, once the temperature reached 580 °C, the temperature was increased to 600 °C directly. For experiment 3, after 580 °C, the target growth temperature is 605 °C instead of 600 °C. The temperature increasing rate was roughly schematically illustrated in Fig. 3l. In addition, to avoid electron-beam damage on liquid Bi under 300kV, all *in situ* TEM images in this experiment were acquired at low magnifications with the condition of low dose rates (< ~10^3 e·nm^{-2}·s^{-1}). A higher dose rate induces severe damage to liquid Bi droplets.

An aberration-corrected environmental TEM (ETEM, Titan from Fisher Thermal, USA) was employed at 300 kV for high-resolution TEM (HRTEM) imaging, bright-field (BF) imaging and select area electron diffraction (SAED) pattern. Another aberration-corrected transmission electron microscope (Titan from Fisher Thermal, USA) equipped with a high-angle annular dark-field (HAADF) detector and an EDS system was employed at 300 kV for HAADF scanning TEM (STEM) and elemental composition analysis. The FEI Helios scanning electron microscopy (SEM) was used to characterize PbSe hierarchical structures at 5 kV.

2. Nucleation and growth of catalyst droplets on PbSe crystal.
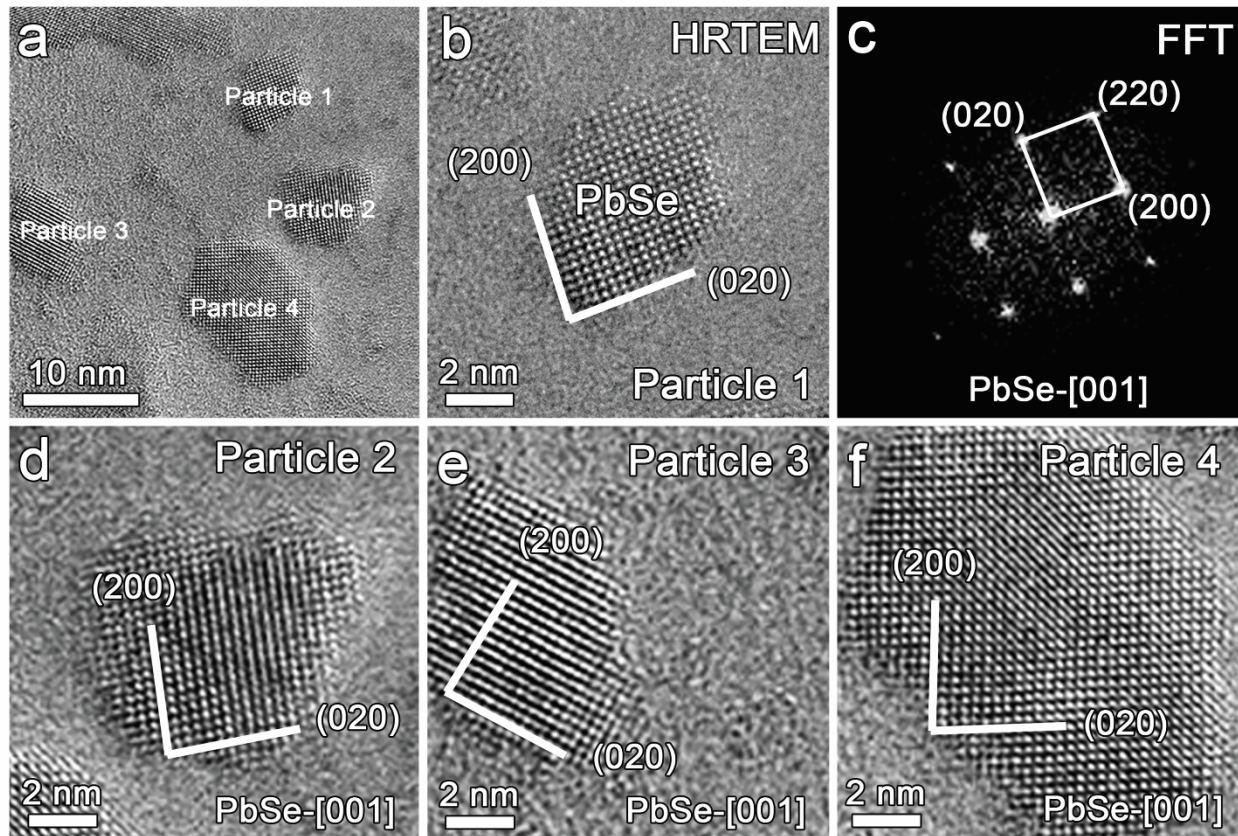

Fig. S1 Formation of PbSe nanoparticles on TEM grids during the heating process. (a) HRTEM image showing PbSe nanoparticles formed at 600°C. (b) Enlarged HRTEM images of the particle 1 in (a). (c) Fast Fourier transform of (b) verifying that the particle 1 is PbSe with zone axis of [001]. (d-f) Enlarged HRTEM images of others particle in (a) with the same orientation of [001].
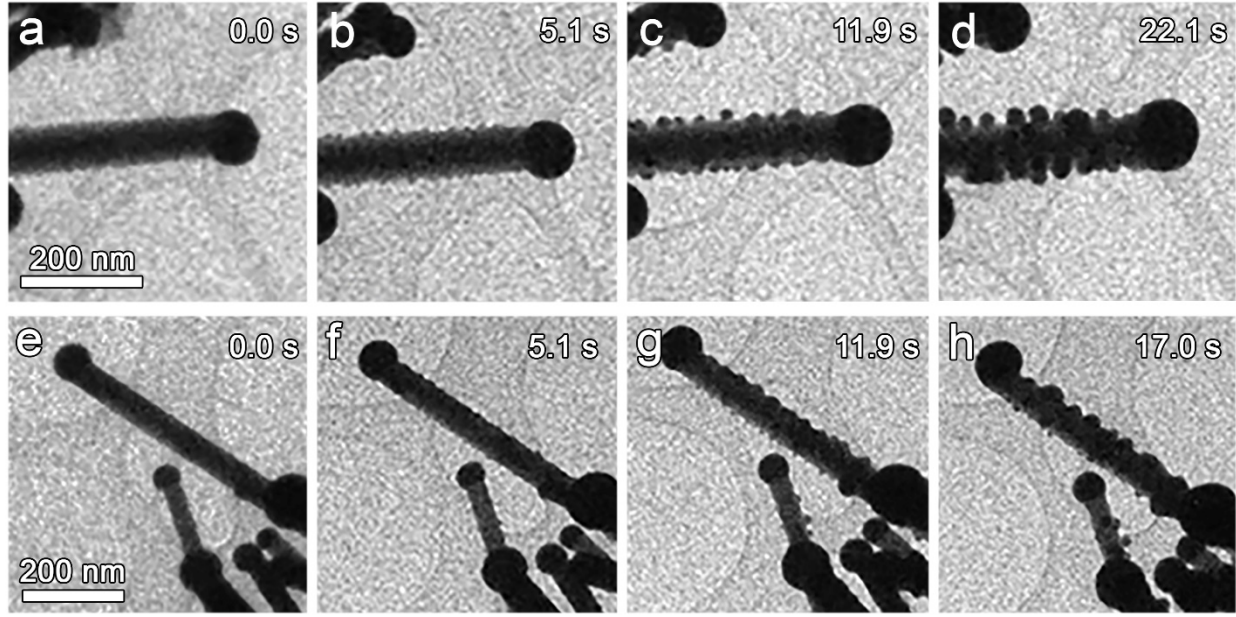
Fig. S2 Two other examples under the condition of Experiment 2, showing the nucleation and growth of catalyst droplets on the sidewall of PbSe wires and higher branch density than wires grown with lower increasing rate of temperature in experiment 1 while the target reaction temperatures are both 600 °C.
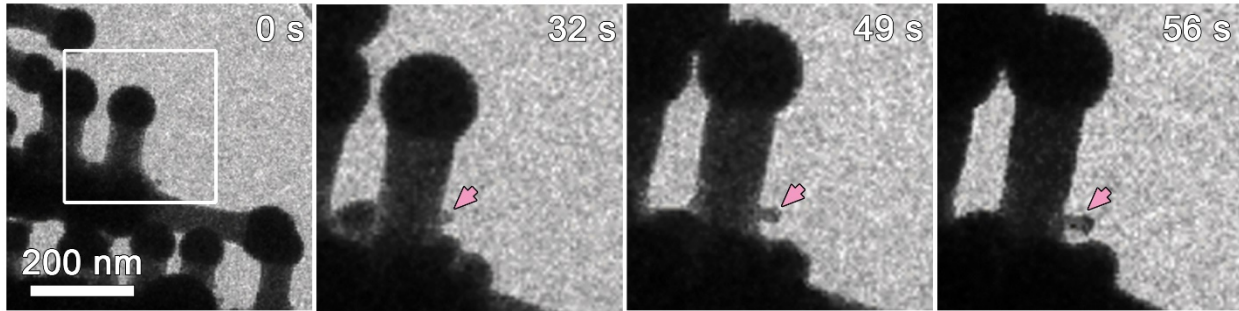

Fig. S3 Time-sequenced BF-TEM images showing the third growth of PbSe on a sidewall of the second growth wire (denoted by pink arrows). 0 s was the first images acquired.

3. The calculated theoretical ratio of the catalyst droplet diameter and the PbSe wire width.

During the stable VLS growth process, based on the balance of surface tensions at the VLS triple-phase junction, we obtain $\mathrm{Sin}\,\alpha = \gamma_{VS} / \gamma_{VL} = R_W / R_S = d_W / d_S$ (Fig. S4). The surface tension of PbSe {200} γ_{VS} is ~0.18 J/m² [1]. The vapor/liquid surface tension γ_{VL} of the pure Bi liquid is ~ 0.35 J/m² [2, 3], which

should be slightly different from the actual surface tension of the liquid catalyst because Pb and Se elements were detected in the catalyst droplet (Fig. S6). The estimated theoretical ratio of $d_W / d_S \approx \gamma_{VS} / \gamma_{VL} = 0.51$.
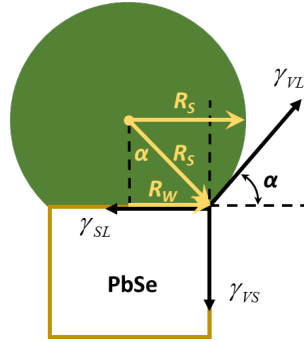

Fig. S4 The relationship between geometrical size and surface tensions at the VLS trip-phase junction during the stable VLS growth process.

4. Evolution of PbSe wire width during the growth process

There are four types of wire width evolution processes.

Type I (increased wire width at $I_{L/S}$): The wire grew thicker and thicker at the $I_{L/S}$ leading to non-uniform width (Fig. S5a-d). With continuous condensation of Bi vapor into the Bi catalyst droplet (Fig. S5a-d), the size of the droplet increased from 226 nm to 293 nm. Correspondingly, the wire size increased during growth (growth type I) and steps formed on the sidewalls of the wires (taper shape, Fig. S5a-e). [4] Because the experiments were carried under an isothermal condition at 600°C and enough catalyst and precursor powders were supplied, Bi liquid droplet catalyst kept growing during the PbSe NW growth process, leading to the increase of wire width at $I_{S/L}$ [5, 6].

Type II (decreased wire width at $I_{L/S}$): In in-situ low mag TEM experiments, the cell is not sealed. After a period of time of the wire growth, Bi vapor depleted slowly into the exhaust system of environmental TEM. The Bi droplet started to evaporate and its size decreased leading to thinner PbSe wire growth and wire width decreased from 154 nm to 138 nm (Fig. S5f-J) at $I_{S/L}$ [5, 6].

Type III (increased wire width at early grown end): Due to a large amount of precursor powers next to the early grown end of the wire (Fig. S5k-n), precursor vapors were deposited on PbSe NW sidewalls near the early grown end, beside absorption by the liquid catalyst droplet. While maintaining a constant diameter of the liquid catalyst droplet (80nm, Fig. S5k-o), the wire at the early grown end grew thicker due to the continuous deposition of PbSe vapor on NWs sidewalls.

Type IV (uniformly increased wire width (Fig. S5p-t)): Due to the synergistic effect of the coarsening of the liquid catalyst sphere (from 46 nm to 109 nm, Fig. S5p-T) and continuously deposition of PbSe vapor on NWs surfaces, the wire grew uniformly thicker while growing along [001], *i.e.*, the combined results of the type I and the type III NWs.

Therefore, the width evolution models are mainly determined by the amount of precursor and catalyst vapors (PbSe and Bi) supplied in experiment and all four kinds of width evolution models demonstrated that the NWs grew horizontally and vertically synchronously with either a uniform or non-uniform width change in our *in situ* TEM experiments.
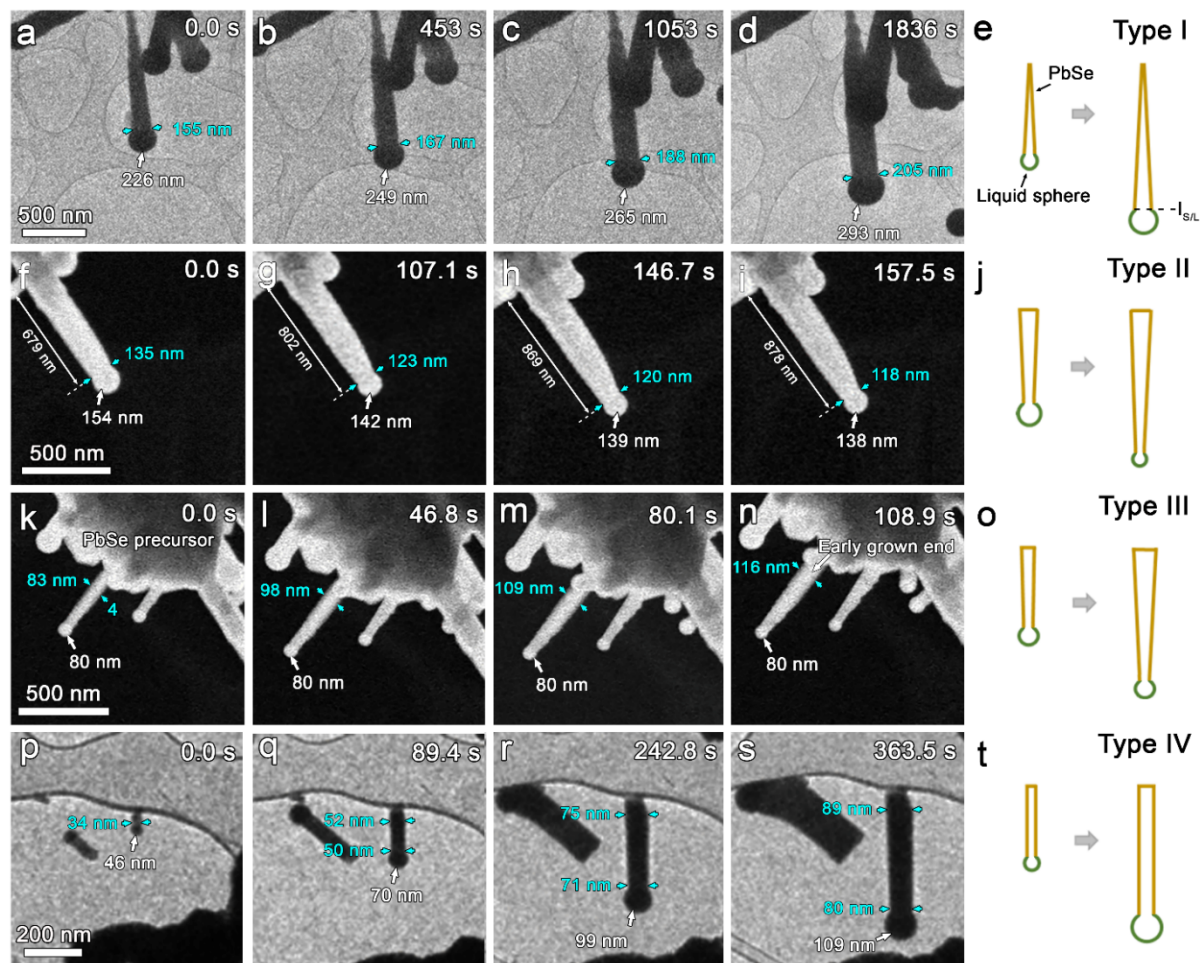
Fig. S5 Size variation of liquid catalyst droplets and PbSe wire width during the in-situ growth process. Various models of PbSe nanowires width growth detected in the in-situ LM TEM experiment at 600 °C. (a-e) Increased wire width at $I_{L/S}$, induced by growth of liquid catalyst sphere, defined as type I. (f-j) Decreased wire width at $I_{L/S}$, induced by shrink of liquid catalyst sphere, defined as type II. (k-o) Increased wire width at early grown end, defined as type III. (p-t) Uniformly increased wire width, defined as type IV.

5. Structure and composition analysis of branched wires

To identify the structure of hierarchical PbSe wires, we further did ex-situ characterization of the wires (Fig. S6). Fig. S6a-b shows the same PbSe branched structure after the second growth and the third growth, showing the variation of width of 1st, 2nd, and 3rd wires (Fig. S6a-b). By tilting to different angles, SEM images verified that the 2nd and 3rd wires grew on {200} sidewalls of 1st and 2nd wires (Fig. S6b-c),

respectively, with the same crystal orientation (Fig. S6e-g), indicating that the PbSe branched structure is a single crystal. Therefore, based on the above SEM and SAED analysis and our previous results [7], we conclude that the PbSe wires grew along the <001> direction with four sidewall surfaces of{200} planes, and the branches grew on {200} sidewall surfaces of PbSe wires. The unchanged wire width from room temperature to ~600 °C indicates that the wires are faceted with four {200} sidewalls at high temperature (Fig. S7). EDS spectrum (Bi peeks in Fig. S6i) and line scan (Fig. S6j) verified that the Bi liquid catalyst droplet contains ~4.1 at.% of Se and ~5.5 at.% of Pb. This observation is different from our previous experiment result that no Se element was detected in liquid catalyst droplets under the environment of a mixed forming gas 5% H_2 in N_2 [7]. This is because gas environment of 5% H_2 in N_2 was used in previous study instead of pure N_2. Based on phase diagram (Fig. S8), both Pb and Se have certain solubilities in Bi liquid at ~600 °C. However, with H_2, most of Se precursors become H_2Se, because Se can easily react with H_2 forming H_2Se [7]. Without H_2, enough Se exists to diffuse in catalyst liquid drop.
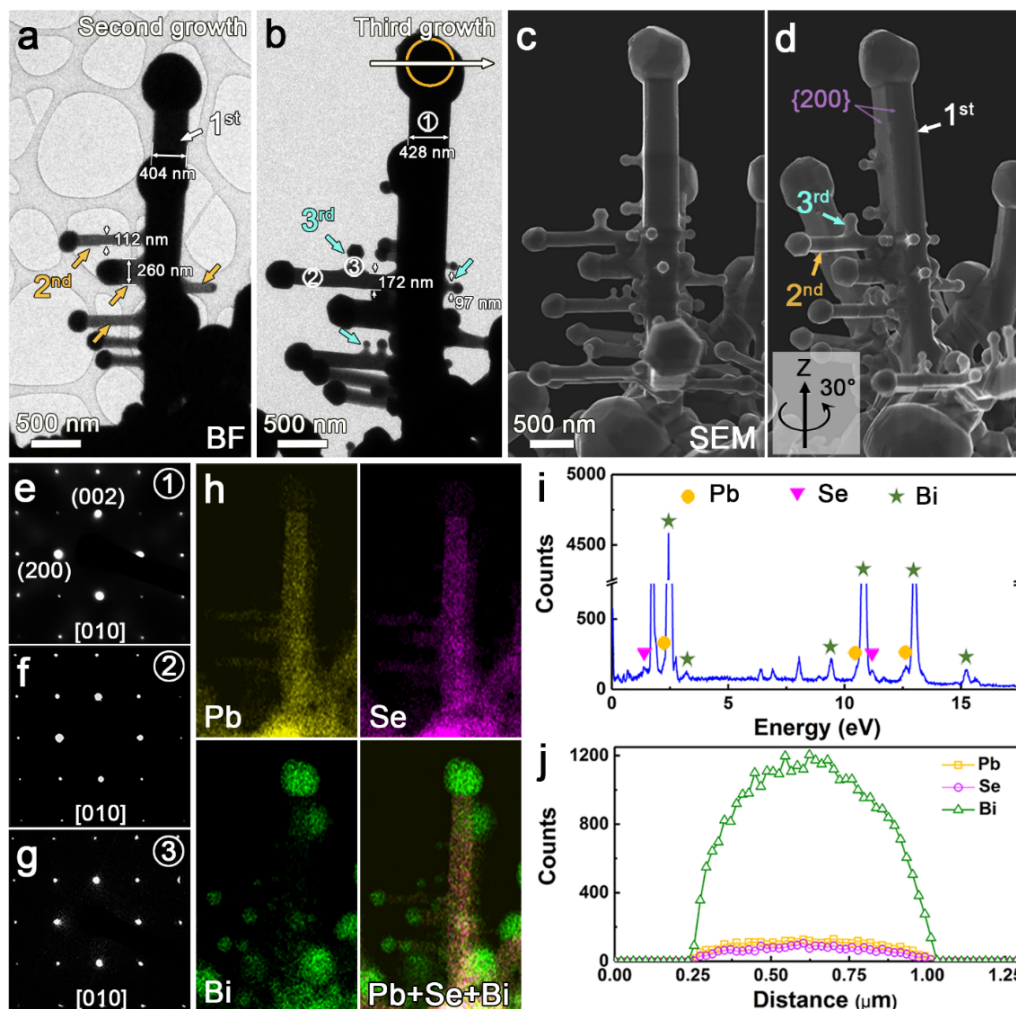
Fig. S6 Branched structures of PbSe after VLS multi-step growth. (a-b) TEM images of the same PbSe branched structure during the second growth and after the third growth. The image of (a) was acquired at the end of the second growth. (c-d) SEM images of the same PbSe branched structure at different title angles showing that the third growth of PbSe wires grew on the 1st and 2nd PbSe wires simultaneously. (e-g) SAED patterns of the 1st, 2nd, and 3rd PbSe wires in (b) showing that three kinds of wires presented the same orientation. (h) EDS mapping of the branched structure in (b). (i-j) EDS spectrum of the yellow-circled area and the line scan along the white arrow direction in (b), respectively, showing the catalyst droplets consisted of Bi, Pb, and Se, and Bi element dominated. The atomic percentages of Se and Pb are ~ 4.1 at.% and ~ 5.5 at.% in (i), respectively.
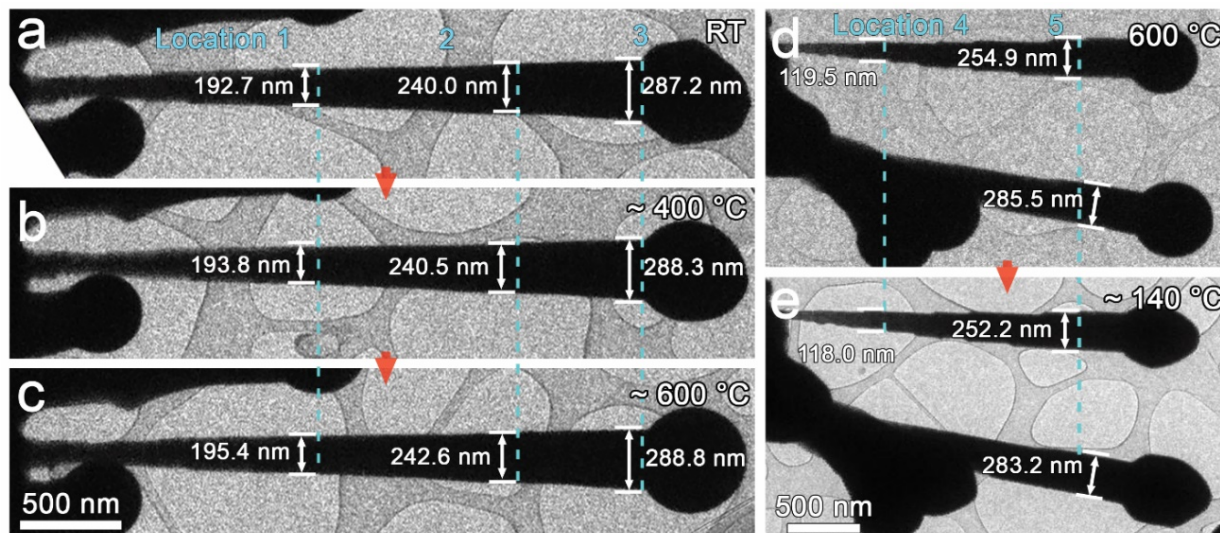
Fig. S7 Analysis of wire size change based on the same wire at various temperatures. (a-c) TEM images of the same wire at room temperature, 400 °C, and 600 °C, showing wire size increased ~0.4 % and ~0.6 % from room temperature to 400°C and from 400 °C to 600 °C, respectively. In total, wire size increased ~1% from room temperature to 600°C. (d-e) TEM images of the same wire at 600 °C and 140 °C, showing wire size decreased 0.7 % from 600 °C to 140 °C. The thermal expansion is ~1% for PbSe from room temperature to 600 °C [8], therefore, there almost no shape variation of PbSe wires during various heating temperatures.
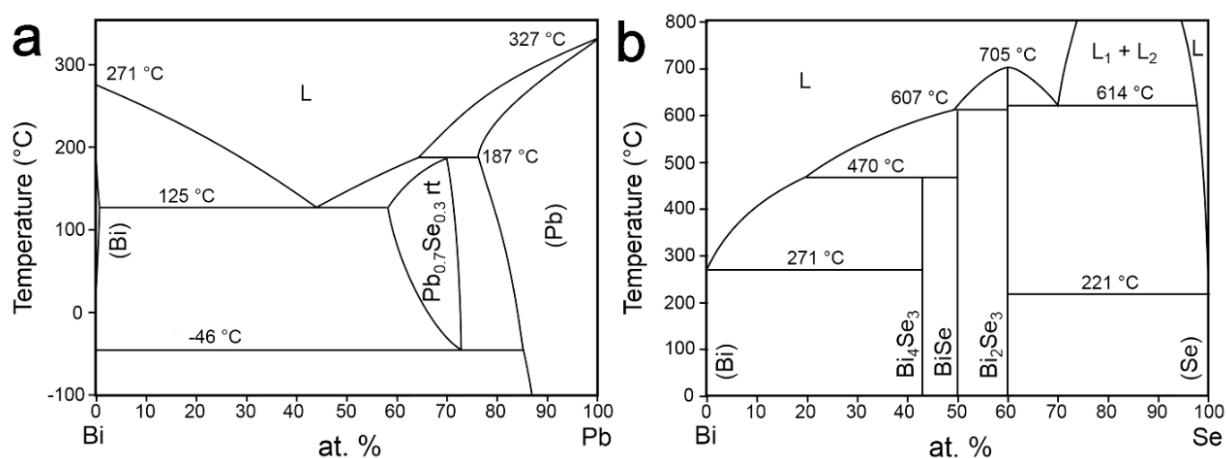

Fig. S8 Binary phase diagrams. (a) Bi-Pb [9]. (b) Bi-Se [9].

6. Estimation of the equilibrium contact angle between the Bi liquid catalyst droplet and the sidewalls of PbSe wire

Based on the in-situ experimental relationship between the Bi catalyst droplets diameter (d_S) and the PbSe wire width (d_W) during in-situ VLS growth, i.e., $d_W / d_S \sim 0.63$ (Fig. 1l-m) and the surface tension of PbSe {200} (γ_{VS}, ~0.18 J/m²) [1], the estimated γ_{LS} is ~ 0.22 J/m². Since only a small amount of Pb and Se are absorbed in Bi liquid (~ 4.1 at.% Se and ~ 5.5 at.% Pb), we used γ_{VL} of the pure Bi liquid ~ 0.35 J/m² [2,3] to estimate the equilibrium contact angle θ of 96.6Fig. based on the balance of surface tensions, i.e., $\gamma_{LS} - \gamma_{VS} + \gamma_{VL} \cos\theta = 0$.

7. De-wetting process of catalyst liquid thin film

There are two possible mechanisms of Bi droplets formation process during the stage I, i.e. Rayleigh instability [10] and spinodal de-wetting [11-13]. Rayleigh instability is the phenomenon where a cylinder is unstable against surface perturbation and breaks up into individual droplets to reduce the total surface energy. However, we ruled out its involvement in the instability of Bi liquid film because the critical wavelength of Rayleigh instability πD (*D* is wire diameter), which is the minimum wavelength of unstable surface perturbation, is much larger than the periodicity of the Bi droplet array. In addition, the nanowire radius varies by two times along the axis of nanowire but the droplet spacing is roughly constant (Fig. 2a-h), which is inconsistent with Rayleigh instability. If a liquid is not thermodynamically favored to wet a substrate, i.e. it has a nonzero contact angle, the liquid film could be destabilized by the spinodal de-wetting process, in which thermally activated undulation to film thickness grows with time and causes the film to rupture. It generates a de-wetting morphology with a characteristic wavelength analogous to spinodal decomposition [14,15]. Spinodal de-wetting is driven by the long-range force such as van der Waals force across the liquid film, accounting which the free energy of the liquid film can be written as:

$$F = \int \left[\gamma\sqrt{1 + (\nabla h(x,y))^2} + \phi(h) \right] dA \qquad \text{(S1)}$$

where γ is the liquid surface energy, h is liquid film thickness and assumed to be uniform along x and y, and $\phi(h)$ is the effective interaction potential, which describes the interaction between the substrate/liquid and liquid/vapor interfaces. When the film is subject to a small periodic perturbation $\delta h \cos(\vec{k} \cdot \vec{x})$ to its uniform thickness h, its free energy change is

$$\Delta F = \int \left[\frac{1}{2}\gamma k^2 + \frac{1}{2}\phi''(h) \right] \delta h^2 \, dA \tag{S2}$$

after keeping the leading order terms. Equation. S2 shows that a perturbation is energetically favorable to grow and destabilize the liquid film when its wavelength is above a critical wavelength given by

$$\lambda_C = 2\pi\sqrt{-\gamma / \phi''(h)} \tag{S3}$$

Here, Equation. S3 shows that spinodal de-wetting only occurs when the second derivative of $\phi(h)$ with respect to h is negative, as illustrated in Fig. 3g. This is very similar to the condition of spinodal decomposition, which develops at compositions where the second derivative of free energy density is negative [14]. Equation. S1 applies to liquid film on a flat substrate, which is suitable here since the Bi film thickness is much smaller than the nanowire diameter. An estimate of λ_C using the experimental data, which is presented below, finds that it is comparable to the periodicity of Bi droplets observed in the experiment. It supports spinodal de-wetting as a probable mechanism of Bi droplets on the PbSe nanowire.

To estimate λ_C, we write $\phi(h)$ as

$$\phi(h) = \frac{A}{2h^2} - \frac{Ah_0^6}{8h^8} \tag{S4}$$

The first term $\phi(h)$ represents the nonretarded dispersive force across the liquid Bi film, and A is the Hamaker constant. The de-wetting of liquid Bi on PbSe implies a negative A or an attractive force between PbSe/Bi and Bi/vapor interfaces at large separation. The second term $\phi(h)$ represents a Lenard-Jones-type short-range repulsion between the interfaces. The parameter h_0 is the equilibrium liquid film

thickness and satisfies $\phi'(h_0) = 0$. As shown in Fig. 3g, $-\phi''(h)$ is initially negative and continues to rise when h increases upon Bi deposition. The film becomes thermodynamically unstable against spinodal de-wetting once $-\phi''(h)$ reaches a positive regime. At thickness with small $|\phi''(h)|$, however, the growth of surface perturbation is slow because of the small driving force and will be overwhelmed by uniform film growth. We assume that the liquid layer thickness at which Bi droplets were observed to emerge on the nanowire is near the thickness h_m that maximizes $-\phi''(h)$. Given Equation. S4 and $h_m = 4$ nm estimated from the experiment (~ 3-5 nm at ~ 33.8 s, Fig. 2b and k), we find that $h_0 = 2.9$ nm and $-\phi''(h_m) \approx -0.47 A / h_0^4$. The remaining parameters in Equation. S1 can be assessed from the contact angles of Bi droplets measured from TEM. At equilibrium, Bi liquid film of thickness h_0 should coexist with Bi droplets. By applying Young's equation to the contact line between the droplet and continuous liquid film, one can write down $\gamma(1 - \cos\theta) = -\phi(h_0)$, or $\gamma h_0^2 / A = -3 / [8(1 - \cos\theta)]$. Using this relation and the estimate $0 \lesssim \cos\theta \lesssim 1/2$ from the measurement at t = 120 s, we obtain $\lambda_C \approx 16 - 23$ nm from Equation. S3. Kinetically, the liquid surface modulation should be dominated by the fastest growing wave and have a characteristic wavelength larger than λ_C. For example, the wavelength of the fastest growing composition modulation in spinodal decomposition is $\sqrt{2}\lambda_C$ [14]. Considering this, the estimate is in reasonable agreement with the Bi droplet spacing. As the contact angle of the droplets continuously increased during measurement, its equilibrium value is likely larger than the estimate used. Even at the maximal value ϑ = 180°, λ_C (11 nm) is still at the same order of magnitude as the experimental observation. Therefore, the formation of periodically arranged Bi droplets is attributed to spinodal de-wetting.

8. Evolution of partial pressure of Bi vapor and growth species

Based on *in situ* observation, Bi powders underwent dissolving, volatilization, and disappearing at ~ 300 °C. Subsequently, Bi vapor condensed on sidewalls of PbSe wires and Bi droplets started to nucleate, grow, and coalescence. PbSe powders as precursors disappeared at ~ 600 °C. Due to the significant difference of melting point between Bi (271°C [9]) and PbSe (1079°C [16]), we expect that Bi vapor pressure increased significantly after 271 °C (Fig. S9). When supersaturation reached, it condensed on PbSe crystal surface. Correspondingly, the partial vapor pressure of Bi dropped (Fig. S9). The vapor pressure of growth species increased quickly after 600 °C and reached supersaturation for VLS growth of PbSe wires.
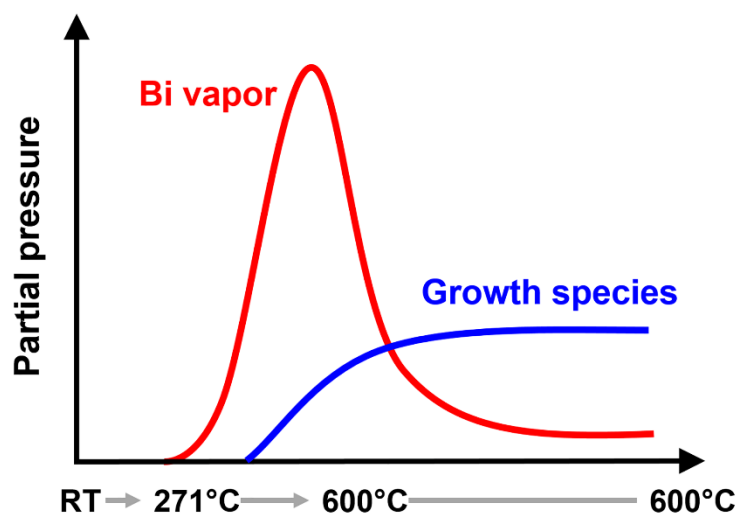
Fig. S9 Hypothesized evolution of partial pressures of Bi and growth species during the heating process.

References

1. Fang, C.; van Huis, M. A.; Vanmaekelbergh, D.; Zandbergen, H. W. *ACS Nano* **2010,** 4, (1), 211-218.
2. Novakovic, R.; Ricci, E.; Giuranno, D.; Gnecco, F. *Surf. Sci.* **2002,** 515, (2), 377-389.
3. Hogness, T. R. *J. Am. Chem. Soc.* **1921,** 43, (7), 1621-1628.
4. Yu, L.; Fortuna, F.; O'Donnell, B.; Patriache, G.; Roca i Cabarrocas, P. *Appl. Phys. Lett.* **2011,** 98, (12), 123113.
5. Schwarz, K. W.; Tersoff, J. *Phys. Rev. Lett.* **2009,** 102, (20), 206101.
6. Ross, F. M. *Rep. Prog. Phys.* **2010,** 73, (11), 114501.
7. Song, M.; Lee, J.; Wang, B.; Legg, B. A.; Hu, S.; Chun, J.; Li, D. *Nanoscale* **2019,** 11, 5874-5878.
8. Skelton, J. M.; Parker, S. C.; Togo, A.; Tanaka, I.; Walsh, A. *Phys. Rev. B* **2014,** 89, (20), 205203.

9.   Massalski, T. B.; Okamoto, H.; Subramanian, P. R., *Binary alloy phase diagrams*. 2, illustrated, reprint ed.; ASM International: 1990; Vol. 1, p 3542.

10.   Rayleigh, J. W. S. *Proc. London Math. Soc.* **1878,** 1, 4-13.

11.   Bischof, J.; Scherer, D.; Herminghaus, S.; Leiderer, P. *Phys. Rev. Lett.* **1996,** 77, (8), 1536-1539.

12.   Herminghaus, S.; Jacobs, K.; Mecke, K.; Bischof, J.; Fery, A.; Ibn-Elhaj, M.; Schlagowski, S. *Science* **1998,** 282, (5390), 916-919.

13.   Xie, R.; Karim, A.; Douglas, J. F.; Han, C. C.; Weiss, R. A. *Physical Review Letters* **1998,** 81, (6), 1251-1254.

14.   Cahn, J. W. *Acta Metall Mater* **1961,** 9, (9), 795-801.

15.   Cahn, J. W. *Journal of Chemical Physics* **1965,** 42, (1), 93-+.

16.   Lin, J. C.; Sharma, R. C.; Chang, Y. A. *Journal of phase equilibria* **1996,** 17, 253-260.